High-dimensional quantum frequency converter

Shilong Liu,[1,*] Chen Yang,[1,*] Zhaohuai Xu,[1] Shikai Liu,[1] Yan Li,[1] Yinhai Li,[1,2] Zhiyuan Zhou,[1,2,†] Guangcan Guo,[1,2] and Baosen Shi[1,2,‡]

[1]*Key Laboratory of Quantum Information, University of Science and Technology of China, Hefei, Anhui 230026, China and Synergetic Innovation Center of Quantum Information and Quantum Physics, University of Science and Technology of China, Hefei, Anhui 230026, China*

[2]*Heilongjiang Provincial Key Laboratory of Quantum Regulation and Control, Wang Da-Heng Collaborative Innovation Center, Harbin University of Science and Technology, Harbin 150080, China*

(Received 17 July 2019; revised manuscript received 25 November 2019; published 23 January 2020)

In high-dimensional quantum communication networks, the quantum frequency converter (QFC) is indispensable as an interface in the frequency domain. For example, many QFCs have been built to link atomic memories and fiber channels. However, almost all QFCs work in a two-dimensional space. It is still a pivotal challenge to construct a high-quality QFC for some complex quantum states, e.g., a high-dimensional single-photon state that refers to a qudit. Here, we firstly propose a high-dimensional QFC for an orbital-angular-momentum qudit via sum-frequency conversion with a flat-top beam pump. As a proof-of-principle demonstration, we realize quantum frequency conversions for a qudit from infrared to visible range. Based on the qudit quantum state tomography, the fidelities of a converted state are 98.29(95.02)%, 97.42(91.74)%, and 86.75(67.04)% for a qudit without (with) accidental counts in 2, 3, and 5 dimensions, respectively. The demonstration is very promising for constructing a high-capacity quantum communication network.

DOI: 10.1103/PhysRevA.101.012339

I. INTRODUCTION

Quantum frequency conversion enables us to change the colors of photons while maintaining their quantum properties [1]. Many quantum frequency converters (QFCs) have been developed based on nonlinear optical processes [2–7]. For example, a polarization-insensitive QFC has been demonstrated to link an atomic ensemble and an infrared photon [8]. Nevertheless, it is still a pivotal challenge to construct a high-quality QFC for some complex quantum states, e.g., a high-dimensional (HD) quantum state [9,10].

A HD single quantum system, sometimes referred to as a qudit, widely existing in single-atom [11], photon [9,10], and superconducting quantum circuits [12], has been widely applied in quantum computations and communications, for example, the Grover search algorithm [11,13]. In a photonic system, one of the widely used qudits is a photon state depicted by a spatial degree of freedom (DOF), i.e., orbital angular momentum (OAM) $|\varphi\rangle_d = \sum_{\ell=0}^{d-1} c_\ell |\ell\rangle$ [14], where $|\ell\rangle$ refers to a state with a topological charge of ℓ; $c_\ell (\sum c_\ell^2 = 1)$ represents amplitude occupations on each eigenstate. During the last decades, great investigations have harnessed the unbounded dimension of qudit in quantum information processing [9,10,15]. For example, in multilevel quantum key distribution, qudits show unique advantages, not only in increasing information capacity but also in strengthening noise tolerance [16–18]. Very recently, some special fibers that could support more OAM modes are being developed to explore fiber-based HD-quantum communication [19,20], i.e., superposition OAM states [21] and maximally entangled states [22].

Frequency conversion is a traditional and useful technology in nonlinear and quantum optics that has wide applications in laser source, optical communications, and some quantum protocols. To date, almost all frequency converters (FCs) serve for a qubit in two-dimensional space [5–8]; it is still a key challenge to construct a high-quality FC serving a qudit, for example, a FC for an OAM superposition state of $(|0\rangle + |1\rangle + |2\rangle)/\sqrt{3}$. The main difficulty is that the conversion efficiency (CE) of FCs usually strongly depends on the topological charge $|\ell|$ (decreasing exponentially with $|\ell|$ [2–4,23–25]). This drawback prevents one from building up a high-fidelity interface between photonic qudits in the different frequency domains. For example, in quantum networks with both quantum memories and fibers, most atomic-based quantum memories operate in the visible wavelength [26–28], while the fiber networks connecting distributed quantum memories usually work in the telecom band in order to minimize the transmission loss [29,30]. Therefore, it is necessary to interface different systems in quantum communication networks by using a QFC. Many works try to balance conversion efficiency for different values of ℓ, for example, using a short nonlinear crystal [31] or optimizing an input spatial profile [25]; however, it reduces the overall CE.

In this work, we first construct a HD-QFC for an OAM qudit. The significant process achieved here is to use a flat-top beam as a strong classical pump instead of a traditional Gaussian pump [2,3,32]. We get an approximate analytic expression of CE for a flat-top pump. Here, the CE is insensitive

*These authors contributed equally to this work.
†zyzhouphy@ustc.edu.cn
‡drshi@ustc.edu.cn

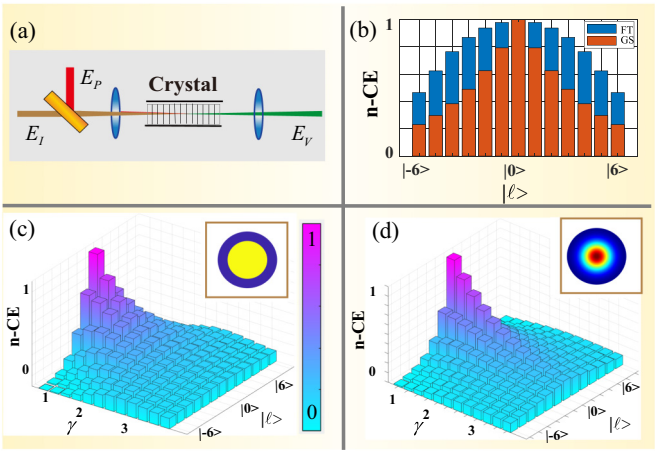

FIG. 1. The conversion efficiency (CE) for HD-QFC. (a) The simple regime of a sum-frequency generation. (b) The normalized CEs (n-CEs) vs different OAM laser pump of Gaussian and flat-top beam, respectively. (c, d) The distributions of the c-CEs vs different beam waist ratio γ, where the inputs are the Gaussian and flat-top beams, respectively. In the simulation, the wavelengths are 794, 1550, and 525 nm for the pump, input, and output, respectively; the beam waist is 100 μm for the input signal photon; for the strong pump laser, the beam waist for the Gaussian or beam size of flat-top sets is 100 μm; and the length of the crystal (PPKTP) is 10 mm.

to the topological charge of the input states. Besides, there is no significant decrease in unit nonlinear conversion efficiency by comparing with previous various QFCs [2–4,23]. As a proof-of-principle demonstration, we realize quantum frequency conversions of a photonic qudit in dimensions of 2, 3, and 5 from the infrared to visible range in the low-power pump regime, where the fidelities of converted states are 98.29%, 97.40%, and 86.75%, respectively. Our method would be valid for other wavelengths. The demonstrated HD-QFC fills an indispensable gap toward interference of different high-dimensional systems in the frequency domain.

II. BUILD A MODE-INDEPENDENT HD-QFC

The second-order nonlinear process, i.e., sum-frequency generation (SFG), can be used to build a high-quality frequency convertor that connects photon state in the frequency domain. In a frequency up-conversion process, i.e., SFG in Fig. 1(a), three waves are interacting with each other in a nonlinear crystal. E_P is the strong classical pump beam; E_I and E_V represent input signal and output photons. During this process, the energy ($\omega_P + \omega_I = \omega_V$), the linear momentum ($k_P + k_I + 2\pi/\Lambda = k_V$), and the OAM ($\ell_P + \ell_I = \ell_V$) are all in conservations.

For a qudit defined in a subspace of $\Re \in \{-[d/2], ..., [d/2]\}$, the entire nonlinear conversion process can be described in an effective Hamiltonian [2,4,25]:

$$\hat{H}_{\text{eff}} = \sum_{\Re} i\hbar\xi_\ell(\hat{a}_{I,\ell}\hat{a}^\dagger_{V,\ell} + \hat{a}^\dagger_{I,\ell}\hat{a}_{V,\ell}), \tag{1}$$

where $\hat{a}^\dagger_{I,\ell}$ and $\hat{a}^\dagger_{V,\ell}$ represent the creating operations of the infrared and visible OAM eigenstate $|\ell\rangle$, and ξ_ℓ is proportional to the product of pump and the second-order susceptibility $\chi^{(2)}$. During a nonlinear FC process, the evolution of annihilation operations ($\hat{a}^\dagger_{\{I,V\},\ell}|0\rangle$) can be given in Heisenberg picture:

$$\begin{bmatrix}\hat{a}_{I,\ell}(\tau)\\ \hat{a}_{V,\ell}(\tau)\end{bmatrix} = \begin{bmatrix}\cos(\xi_\ell\tau) & -\sin(\xi_\ell\tau)\\ \sin(\xi_\ell\tau) & \cos(\xi_\ell\tau)\end{bmatrix}\begin{bmatrix}\hat{a}_{I,\ell}(0)\\ \hat{a}_{V,\ell}(0)\end{bmatrix}. \tag{2}$$

Here, τ is the traveling time of the photon through the nonlinear crystal. The HD-QFC can be seen as a spatial beam splitter (BS) for OAM states in the frequency domain [33], where we can regard $\cos^2(\xi_\ell\tau)$ and $\sin^2(\xi_\ell\tau)$ as the transmission probability of the photon in the original frequency and the reflectance probability of the photon in up-converted frequency, respectively. One should note that such a spatial BS is mode dependent, since ξ_ℓ is dependent on $|\ell|$.

For the input being a weak coherent laser, one can regard $\cos^2(\xi_\ell\tau)$ as the conversion efficiency, which is proportional to the normalized conversion efficiency (n-CE): $\eta_P = P_V/P_I P_P$. The n-CE can be calculated via nonlinear coupled-wave equations [34,35]. It can be found that the n-CEs for different OAM lasers are strongly dependent on the input pump beam profile. Generally, for a Gaussian beam, the n-CE can be given as [4,23]

$$\eta_{p-G} = \frac{16\pi^2 d_{\text{eff}}^2 L 2^{|\ell|}}{\varepsilon_0 c n_I n_V \lambda_V^2 \lambda_P} h(|\ell|, \xi), \tag{3}$$

where L is the length of the crystal, d_{eff} is the effective coefficient of the crystal, $n_{V,I}$ belongs to the refractive index for up-converted and input fields, ε_0 and c represent the vacuum permittivity and the light speed in the vacuum, and $h(|\ell|, \xi)$ is an integral function associated with the focusing parameter $\xi = L/2\pi w_0^2/\lambda_P$ and topologic charge $|\ell|$. The n-CEs for an OAM state from -6 to 6 are shown in Fig. 1(b) (red bars). We can find that the n-CEs will decrease rapidly along with the increases of $|\ell|$. However, the n-CEs would be balanced if the input was a flat-top beam (FTB). The FTB has a flat intensity profile and flat phase ($\ell = 0$) in some well-defined region, and zero elsewhere:

$$I_{\text{FTB}}(\rho) = \begin{cases}1 & |\rho| \leqslant w_{\text{FTB}}\\ 0 & |\rho| > w_{\text{FTB}}\end{cases}, \tag{4}$$

where w_{FTB} is the width of the FTB, and ρ ($=\sqrt{x^2+y^2}$) represents the spatial transverse coordinates. By inserting the flat-top beam into the coupling equation, one can get the n-CEs for an OAM eigenstate:

$$\eta_{p-F} = \frac{16\pi d_{\text{eff}}^2 2^{|\ell|}}{\varepsilon_0 c n_V n_I n_P \lambda_P^2 w_p^2 |\ell|!} h(|\ell|, \gamma), \tag{5}$$

where the $h(|\ell|, \gamma)$ is an integral function associated with beam waist ratios ($\gamma = w_p/w_i$) and topologic $|\ell|$. The theoretical n-CEs under the FTB are shown in Fig. 1(b) (blue bars). Here, all the parameters are the same as the Gaussian situation. The simulations illustrate that the n-CEs under the flat-top pump tend to be flatter than the Gaussian pump, which is beneficial to build a mode-dependent QFC in an OAM subspace. Also, we studied the n-CEs again with a different beam ratio of γ, which is shown in Figs. 1(c) (flat top) and 1(d) (Gaussian). Two three-dimensional distributions clearly illustrate that the n-CEs of OAM modes are balanced in the regime of the FTB pump. In addition, the larger the beam size

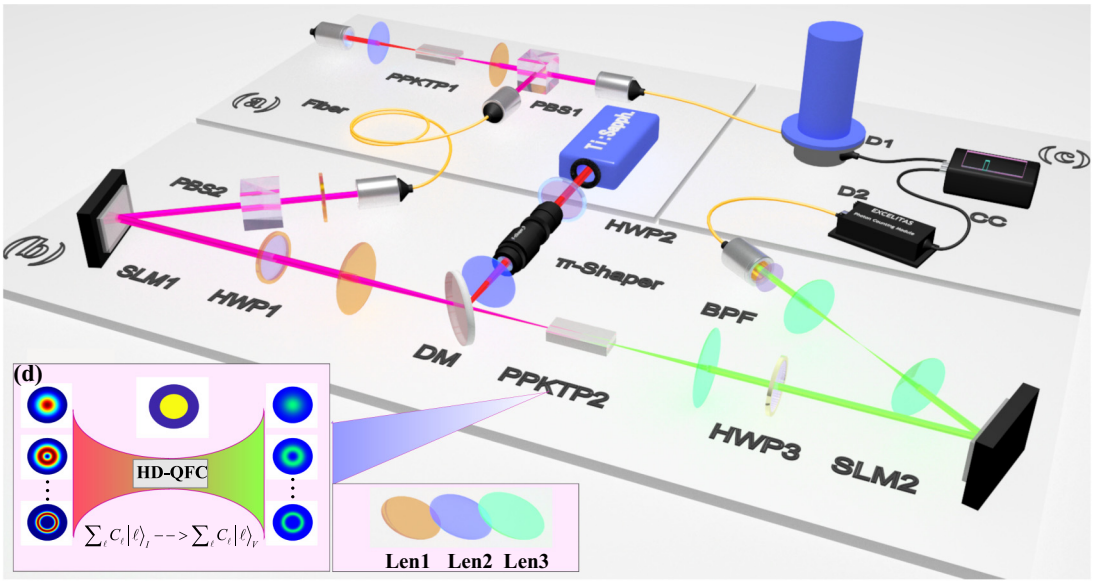

FIG. 2. Schematics of a HD-QFC. (a) Generation of an infrared heralding single-photon state. (b) the HD-QFC for a qudit preparation, conversion, and projection measurement, where the pump is a flat-top beam shaped by a π shaper. (c) The electronic logic modules for correlation measurement. (d) The simple frame for the HD-QFC. PBS: polarization beam splitter; DM: dichromatic mirror; HWP1 (2, 3): half-wave plate for infrared (pump, visible) photon; Len1(2, 3): lens work in infrared (1550 nm), pump (794 nm), and visible (525 nm) bands. SLM1(2): a spatial light modulator for infrared (visible) photons; BPF: bandpass filter; D1: D2: single-photon avalanche diode detector; C.C.: correlation coincidence logic. The classical strong pumps in SPDC and sum-frequency generation are continuous waves.

(γ) of the flat-top beam, the more flat the n-CEs of the OAM state will be, which is reasonable because the FTB is near an ideal plane wave when the beam size is large enough.

The n-CE in Eq. (5) is the ideal situation where the beam profile still stays flat in crystal. However, the flat-top beam will be out of shape due to the diffraction, which is because the flat-top beam is not the solution of the paraxial Helmholtz equation. One could first determine $E_P(\rho, z)$ by the Rayleigh-Sommerfeld diffraction integral [36,37], then numerically simulate the output field E_V via coupling equations, and finally, calculate the quality of the HD-QFC, i.e., fidelity. Fortunately, the FTB shaped by the commercial π shaper maintains a flat profile within 10 mm. Therefore, the approximation is reasonable. (More details can be found in Appendix A.)

III. RESULTS

A. Experimental setup for a HD-QFC

Figure 2 shows an experimental setup of the HD-QFC, which can converts a qudit from infrared to the visible spectrum. Three parts are assigned to state generation [Fig. 2(a)], conversion [Fig. 2(b)], and correlation measurements [Fig. 2(c)], respectively. The infrared heralded single photons are prepared via the spontaneous parametric down-conversion (SPDC) in a type-II quasi-phase-matching nonlinear crystal (PPKTP1, $1 \times 2 \times 20$ mm^3). The beam waist of input with 775 nm is 115 μm at the center of PPKTP1. The infrared 1550-nm photon pairs are collected by an infrared lens ($f =$ 100 mm). The infrared idler photon acts as a heralding signal detected by a superconducting nanowire single-photon detector (SNSPD); the signal photon is collected to the fiber as a source to prepare an arbitrary OAM qudit by a spatial light modulator (SLM1). The heralded infrared single-photon efficiency is 25%. For reducing the accidental coincidence, we add a narrow-band fiber filter of 100 GHz bandwidth at the center of 1550 nm.

For qudit state generation, one can employ amplitude-encoding technology with the help of a SLM [38]. In our recent work [39], we can prepare an arbitrary OAM superposition state $\sum_\ell C_\ell |\ell\rangle$ with high fidelity as listed in the dimension of 7. Following that technology, we first create the phase hologram of a qudit and then load it onto SLM2. The quality of the state can be tested by interference visibility or fidelity with the projection measurements. In preparation, we need to slightly balance the amplitudes for each OAM eigenstate to get rid of the mode-dependent reflective efficiency.

The HD-QFC [Fig. 2(d)] plays the role of a coherent interface connecting the infrared and visible photon via sum-frequency generation, which involves a flat-top beam, and a type-I quasi-phase-matching nonlinear crystal (PPKTP2). In our setup, both a π shaper and a Fourier lens are used to transform a Gaussian beam to be a focused flat-top beam. The basic principle of a π shaper is to shape a Gaussian beam to an Airy disk via the Fourier-Bessel transform: $I_f(\rho) = I_{f0}[J_0(2\pi\rho)/2\pi\rho]^2$ [40]. Here $J_0(2\pi\rho)$ is the first kind and zero-order Bessel function and I_{f0} is the normalized factor. The beam profile of the flat top can be seen in Appendix A.

B. Conversion efficiency and coherence of qudits

Figure 3(a) shows the relationship between the power CE and the input pump power for OAM eigenstates $|0\rangle_I$, $|1\rangle_I$, and $|2\rangle_I$, where the insets are corresponding theoretical intensity distributions. In Fig. 3(a), the power CE is proportional to the input pump's power. Therefore, one can calculate the

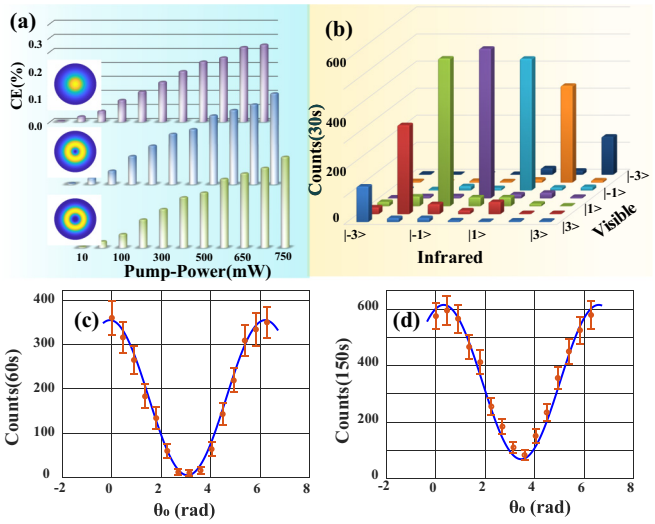

FIG. 3. The mode conversion efficiency of HD-QFC and interference curves for the qudit in the dimension of 2 and 3. (a) The mode conversion efficiencies vs the input pump power for inputs of $|0\rangle$, $|1\rangle$, and $|2\rangle$. (b) The coincidence between infrared and visible photons for single OAM eigenstates in subspace $\{-3, \ldots, 3\}$, where the accidental count is 6. (c, d) Coincidences minus the accidental counts are recorded by scanning the phase angle in a spatial light modulator (SLM2), where the projection states are $(e^{i\theta_0}|-1\rangle + |1\rangle)^{\dagger}$ and $(|-1\rangle + e^{i\theta_0}|0\rangle + |1\rangle)^{\dagger}$ for a two- and a three-dimensional qudit state, respectively. Each coincidence data for (b), (c), and (d) are recorded by 30, 60, and 150 s.

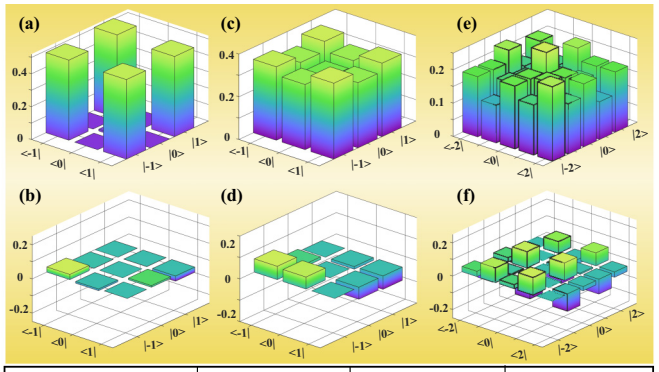

d/Fidelity	*d=2*	*d=3*	*d=5*
Gaussian-beam-T	100%	92.47%	83.36%
Flattop-beam-T	100%	99.88%	99.80%
Flattop-beam-E	98.29(95.02)%	97.42(91.74)%	86.75(67.04)%

FIG. 4. The reconstructed density matrix and the fidelity for a qudit in three- and five-dimensional space via quantum state tomography. (a, b) The real and imaginary parts of the density matrix for a qubit state $(|-1\rangle + |1\rangle)/\sqrt{2}$. (c, d) The real and imaginary part of the density matrix for a three-dimensional state $|\varphi\rangle_{\Re=3} = (|-1\rangle + |0\rangle + |1\rangle)/\sqrt{3}$. (e, f) The situations of a qudit $|\varphi\rangle_{\Re=5} = (|-2\rangle + |-1\rangle + |0\rangle + |1\rangle + |2\rangle)/\sqrt{5}$ in five-dimensional subspace. Each coincidence data for three qudits are recorded at 100 s, 300 s, and 300 s, respectively. The corresponding accidental counts are 16, 20, and 40, where the single counts in idler ports are 0.4, 0.4, and 1 Mhz. In our experiment, the photon counts can be adjusted by increasing the input power in PPKTP1. The inserted table shows the qudit fidelities for $d = 2$, 3, and 5 via Gaussian or flat-top beam pump, where the Gaussian-beam-T and flat-top-beam-T are theoretical predictions based on the nonlinear coupling equations. The flat-top-beam-E is the experimental reconstructed results without (with) accidental counts based on the state tomography.

average normalized nonlinear CE (n-CE) ($=P_V/P_I P_P$): 0.37%/W, 0.42%/W, and 0.33%/W for the OAM eigenstate of $\ell = 0$, 1, and 2, respectively. On the contrary, the previous schemes with a Gaussian pump show a significant difference in n-CE among these eigenstates [2,23,25] (also see the Table I in Appendix A), for example, 1.5%/W, 0.5%/W, and 0.3%/W for the same states, respectively [23]. The theoretical n-CE for two types of pumps can be calculated by the coupled-wave equations [34] (also see Appendix A). Both theory and experiments show the n-CE are nearly equal for three eigenstates in our scheme, which enable us to build a high-quality HD-QFC at least in a five-dimensional subspace.

Figure 3(b) depicts the coincidences between the input infrared and converted visible photons, where the topologic charges of the input and projected states are set to be -3 to 3. For quantifying crosstalk, we calculate the signal-to-noise ratio ($=\sum_i C_{i,i}/\sum_{i,j} C_{i,j}$) in OAM space being 90.53(83.47) $\pm$ 0.68% without (with) accidental counts, where the error bars were estimated assuming the data follows Poisson's distribution. Due to the mode-dependent collection efficiency in the projection measurement [41], the coincidence for higher-order modes decreases quickly. Nevertheless, one can construct a HD-QFC for a qudit consisting of several symmetric low-order modes, for example, a five-dimensional qudit.

For a qudit defined in a subspace $\Re$, an ideal output state after HD-QFC can be written as

$$|\varphi\rangle_{\Re} = \frac{1}{\sqrt{d}} \sum_{\ell=-[d/2]}^{[d/2]} |\ell\rangle. \tag{6}$$

Usually there are some relative phases $e^{i\phi_\ell}$ between different OAM eigenstates due to mode dispersion [42]. For testing the existing phases, we perform projection measurements in SLM2 (in Fig. 2) via scanning one of the phases to get coincidence interference curves, which should be given by $|d - 1 + e^{i\phi_\ell}|^2$ for an ideal qudit.

For a two-dimensional state, the theoretical coincidence should be $1 + \cos(\phi_\ell)$; the visibility ($= C_{\text{Max}} - C_{\text{Min}}/C_{\text{Max}} + C_{\text{Min}}$) could be up to 100%. Figure 3(c) shows the experimental data for a two-dimensional state $(|-1\rangle + |1\rangle)/\sqrt{2}$, where each of data is recorded per 60 s without the accidental counts. The experimental visibility is $95.32 \pm 2.60\%$ according to the solid fitted line, where the error bars were estimated by assuming coincidences follow Poisson's distribution. Figure 3(d) is the situation of a three-dimensional qudit, where the visibility is $75.97 \pm 4.58\%$. For a three-dimensional qudit, the theoretical visibility is 80%. Because of a relative phase between different modes [42], the fitted line appears as a very small shift. During the state preparation, we can make up for this small phase by adjusting the input phase hologram in SLM1. Nevertheless, the visibility illustrates that the qudit states have good coherence.

C. Quantum state tomography of qudits

We evaluate a photonic qudit in subspace $\Re$ via the qudit quantum state tomography (QST) after HD-QFC [43]. We need to make a mode projection measurement in the complete mutually unbiased bases (MUBs). For a qudit defined in the prime dimension, the used MUBs can be generated by a discrete Fourier transformation [44]:

$$\{|a_m^j\rangle\} = \left\{ \frac{1}{\sqrt{d}} \sum_{n=0}^{d-1} \omega_d^{(jn^2+nm)} |n\rangle \right\}, \tag{7}$$

where j indexes the group of the MUBs, and m indexes the superposed OAM states for each set [39,44] (also see Appendix B). After loading the phase hologram of MUBs [Eq. (7)] in SLM2, we perform correlation measurements between infrared and visible photons. Using the maximum-likelihood estimation method, we reconstruct the density matrix of a qudit, which is shown in Fig. 4. Figures 4(a) and 4(b) are the real and imaginary parts of the density matrix of the qubit state, where we perform QST in two-dimensional subspace $|\varphi\rangle_{\Re=2} = |-1\rangle + |1\rangle/\sqrt{2}$. Figures 4(c) and 4(d), and Figs. 4(e) and 4(f), are the situations of $|\varphi\rangle_{\Re=3}$ and $|\varphi\rangle_{\Re=5}$ in their subspaces, respectively.

Usually, we tend to calculate the fidelity by $F = \mathrm{Tr}[\sqrt{\sqrt{\rho}\rho_{\exp}\sqrt{\rho}}]^2$ between theoretical ($\rho = |\varphi\rangle_{\Re}\langle\varphi|_{\Re} = 1/d \sum_{j,k=-[d/2]}^{[d/2]} |j\rangle\langle k|$) and experimental density matrices to evaluate the quality of the QFC. The fidelities without (with) accidental counts are $98.29(95.02) \pm 1.55\%$, $97.42(91.74) \pm 1.11\%$, and $86.75(67.04) \pm 1.80\%$ for a two-, three-, and five-dimensional qudit. The theoretical fidelities of QFC with a Gaussian and a flat-top beam as a pump are summarized in a table at the bottom of Fig. 4.

The fidelities are a bit low for a qudit in a five-dimensional subspace because of the low signal-to-noise ratio (SNR). Also, the SNR will lower the visibility during the interference measurements. SNR is derived from two counts; the accidental and the signal coincidence counts. Generally, the less the accidental counts or the more signal coincidence counts, the higher the SNR, producing a higher fidelity qudit. The accidental counts mainly come from background electric noise, stray light, and spontaneous radiation noise, which approaches a constant when input parameters are fixed. However, the mode signal coincidence counts mainly depend on the conversion and collection efficiency. In our regime, the conversion efficiency is equal at last in a five-dimensional subspace $\{-2, -1, \ldots, 2\}$, while the effective collection efficiency is strongly dependent on the dimensions if one uses the mode projection measurement [45,46]. For example, for a two-dimensional state, $(|-1\rangle + |1\rangle)/\sqrt{2}$, the state will be $(|-2\rangle + |0\rangle + |0\rangle + |2\rangle)/4$, where we collect only $|0\rangle$ due to a single-mode filter. Therefore, only 50% of the photons are collected. For a qudit in d subspace, the effective coupling photon occupies only $1/d$. So in our experiment, the fidelity of a qudit in a five-dimensional subspace mainly comes from the natural dimension-dependent collection efficiency during the projection measurement. Therefore, subtracting the accidental counts is reasonable during the state constructions, especially for a qudit in higher dimensions. Besides, some minor factors could affect fidelity during the QST, i.e., the imperfect input state, mode-dependent losses (transmission) [47], and mode-dependent collection [41]. Nevertheless, we give two results in visibility and fidelity, with and without accidental counts.

IV. DISCUSSION

Employing the pump manipulating technology, we firstly build a high-quality HD-QFC connecting two photons in different colors. Using a focused flat-top beam as a pump not only keeps the input beam profiles but also has a normal normalized conversion efficiency. In the future, we can build a higher-dimensional QFC to serve for high-dimensional quantum communications. Based on Eq. (5), we could optimize the area of the flat-top beam in the nonlinear crystal. Also, the HD-QFC with a flat-top beam pump presents a unique advantage in image frequency conversion, as it supports the higher-order spatial modes [48]. The technique could also be beneficial to other conversion systems, i.e., spatiotemporal imaging [49] and reversible OAM photon-phonon conversion [50].

Because the current QFC works in a single pass regime, the overall CE is rather low. Nevertheless, one can see that the normalized mode conversion efficiency is comparable with other implementations (see Table I in Appendix A). The total CEs would increase via directly enhancing input pump laser power or placing the crystal in a particular cavity that resonates with a flat-top beam [51]. Recently, some flat-top beam-shaping technique and productions have been proposed to work in higher power [52,53]. Another convenient way is to employ a high-peak-power pulse as a classical pump, where the photon pairs should also be generated from a pulse laser pump.

ACKNOWLEDGMENTS

This work is partially supported by the Anhui Initiative in Quantum Information Technologies (Grant No. AHY020200), the National Natural Science Foundation of China (Grants No. 61435011, No. 61525504, No. 61775025, No. 61405030, and No. 11934013), the China Postdoctoral Science Foundation (Grants No. 2016M590570 and No. 2017M622003).

APPENDIX A: CONVERSION EFFICIENCY UNDER THE PUMPS OF GAUSSIAN AND FLAT-TOP BEAMS

For a frequency up-conversion process, three waves are interacting with each other in a nonlinear crystal. When the pump has strong power, the frequency up-conversion process can be calculated by the nonlinear coupled-wave equations [34]:

$$\begin{aligned} \frac{\partial E_I(\vec{\rho}, z)}{\partial z} &= \frac{i}{2k_I} \nabla_\rho{}^2 E_I(\vec{\rho}, z) + K_I E_P^*(\vec{\rho}, z) E_V(\vec{\rho}, z) e^{i\Delta k z}, \\ \frac{\partial E_V(\vec{\rho}, z)}{\partial z} &= \frac{i}{2k_V} \nabla_\rho{}^2 E_V(\vec{\rho}, z) + K_V E_P(\vec{\rho}, z) E_I(\vec{\rho}, z) e^{-i\Delta k z}, \end{aligned} \tag{A1}$$

where the pump E_P, input signal E_I, and the up-converted output E_V have angular frequencies of ω_P, ω_I, and ω_V, respectively, and k_I and k_V represent the wave vector of the input

TABLE I. Conversion efficiency of various OAM states.

Dimensions	Configuration	Converted state	N-CE (%/W)	Ref.
$d = 2$	Cavity, 10 mm PPKTP $(1560 + 792 = 525$ nm)	Single-photon state: $\|\ell\rangle + e^{i\phi}\|-\ell\rangle$	3.5 at $\ell = 0$ 1.4 at $\ell = 1$ 0.4 at $\ell = 2$	[4]
$d = 2$	Cavity, 10 mm PPKTP $(1560 + 792 = 525$ nm)	Entangled state: $\|H, \ell\rangle + e^{i\phi}\|V, -\ell\rangle$	1.0 at $\ell = 1$	[2]
$d = 2$	Cavity, 50 mm PPLN $(1560 + 792 = 525$ nm)	Coherent laser: $\|\ell\rangle + e^{i\phi}\|-\ell\rangle$	1.5 at $\ell = 0$ 0.5 at $\ell = 1$ 0.3 at $\ell = 2$	[23]
$d = 2$	Single pass, 10 mm PPLN $(1475 + 803 = 527$ nm)	Coherent laser: $\|\ell\rangle + e^{i\phi}\|-\ell\rangle$	1.8 at $\ell = 0$ 1.3 at $\ell = 1$	[3]
$d = 2$	Single pass, 10 mm PPLN $(1565 + 806 = 532$ nm)	Coherent laser of LG and HG mode	Average CE 10^{-4}	[24]
$d = 3, 5$	Single pass, 10 mm PPKTP $(1550 + 794 = 525$ nm)	Single-photon qudit state: $\|-2\rangle + \|-1\rangle + \cdots + \|2\rangle$	0.37 at $\ell = 0$ 0.42 at $\ell = 1$ 0.33 at $\ell = 2$ 0.24 at $\ell = 3$	This work

infrared and output visible fields. $\nabla_\rho^2 = \partial^2/\partial x^2 + \partial^2/\partial y^2$ is a two-dimensional Laplace operator; $\Delta k = k_P + k_I - k_V - 2\pi/\Lambda$ shows the phase mismatch equation in the wave-vector domain. One can get the output field $E_V(\rho, z)$ via solving coupling Eq. (A1) with the split-step Fourier method. In that case, the output power can be calculated after the nonlinear conversion:

$$P_V(z = L/2) \sim \int_{-L/2}^{+L/2} E_V(z)E_V^*(z)dz, \tag{A2}$$

where L is the length of the nonlinear crystal. The normalized power conversion efficiency (n-CE) can be written as $\eta_p = P_V/P_I P_P$, and the quantum conversion efficiency has the following form: $\eta_q = N_V/N_I = P_V\lambda_V/P_I\lambda_I$, where λ_I and λ_V are wavelengths of input and output photons, respectively. We now discuss two types of up-conversion processes based on the pump beam profile.

(i) The pump is the Gaussian beam. Based on the nonlinear coupling equation, one can get an analytical expression of the n-CE as the input being a Laguerre-Gaussian (LG) mode [4,23]:

$$\eta_{p-G} = \frac{16\pi^2 d_{\text{eff}}^2 L 2^{|\ell|}}{\varepsilon_0 c n_I n_V \lambda_V^2 \lambda_P} h(|\ell|, \xi), \tag{A3}$$

where L is the crystal length, d_{eff} is the effective coefficient of crystal, $n_{V,I}$ belongs to the refractive index for up-converted and input fields, ε_0 and c represent the vacuum permittivity and the light speed in the vacuum, and $h(|\ell|, \xi)$ is an integral function associated with the focusing parameter $\xi = L/2\pi w_0^2/\lambda_P$ and topologic charge $|\ell|$.

(ii) The pump is a flat-top beam. A flat-top beam, i.e.,

$$E_p = \begin{cases} N_0 & r <= w_p \\ 0 & r > w_p \end{cases}, \tag{A4}$$

is a flat intensity in a special area ($r <= w_p$) and zero intensity otherwise ($r > 0$). We can get the normalized N_0 based on the input pump power: $N_0 = \sqrt{P_P/2\pi\varepsilon_0 c n_P w_p^2}$. By the coupling equation, the n-CE can be given by

$$\eta_{p-F} = \frac{16\pi d_{\text{eff}}^2 2^{|\ell|}}{\varepsilon_0 c n_V n_I n_P \lambda_P^2 w_p^2 |\ell|!} h(|\ell|, \gamma), \tag{A5}$$

where all of the parameters are the same as the situation of a Gaussian pump beside the integral function $h(|\ell|, \gamma)$, which can be given in

$$h(\ell, \gamma) = \int_{-L/2}^{L/2}\int_{-L/2}^{L/2} [|\ell|! - \Gamma(1 + |\ell|, b\gamma^2)] \times (1 + ix/Z_I + 1 - iy/Z_I)dxdy, \tag{A6}$$

where $Z_I (= \pi w_i^2 n_I/\lambda_I)$ is the Rayleigh distance of the input infrared light, $\Gamma(n, z)$ represents the incomplete γ function, and $b = 1/(1 + ix/Z_I) + 1/(1 + iy/Z_I)$. Based on Eq. (A5), one can get the n-CEs for different OAM states.

Because the flat-top beam is not the solution of the paraxial Helmholtz equation, the flat-top beam will be out of shape due to the diffraction. In order to get the output E_V, one can first determine $E_P(\rho, z)$ by the Rayleigh-Sommerfeld diffraction integral [36,37]. Then the output field E_V and original E_I can be simulated via Eq. (A1). In that case, we can calculate all of the parameters, i.e., conversion efficiency, state fidelity, and so on.

Figures 5(a) and 5(b) are the theoretical single-pass conversion efficiencies (SPCEs) when the input pump is a Gaussian and a flat-top beam, respectively. We use the split-step Fourier method to solve Eq. (A1) and thus get the corresponding power conversion efficiency. In our scheme, we employ a π shaper to generate an Airy disk and then use a Fourier lens to transfer an Airy disk to a focusing flat-top beam in the Fourier plane [40]. Here the diameter of the pump beam before the π shaper is 4 mm, and the distance between the Fourier lens ($f = 300$ mm) and π shaper is 100 mm. The length of the crystal (PPKTP) is 10 mm. We simulate the distribution of the flat-top beam in the center of the crystal via the Collins diffraction equation [54], which is shown in Fig. 5(c). The red bars in Fig. 5(b) show the experimental SPCE with the

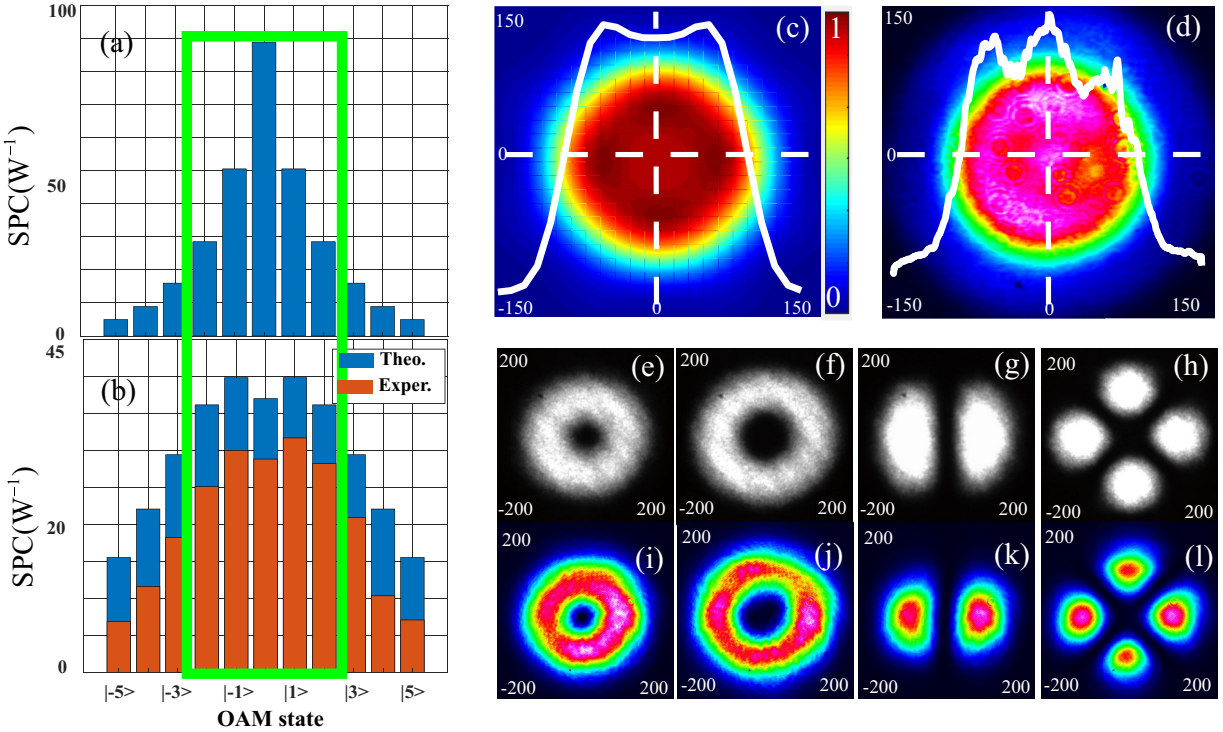

FIG. 5. The conversion efficiency and beam profiles for a high-dimensional frequency converter (HD-FC). (a, b) Conversion efficiency for pumps of the Gaussian and flat-top beam in a single-pass configuration, where the x axes are the same for (a) and (b), which represents the topologic number ℓ of input OAM states. (c, d) The beam profiles for a theoretical and experimental flat-top beam, where the white lines are the one-dimensional distribution along the vertical center of the beam profile. (e, h) The beam profiles of input OAM states. (i, l) The beam profiles of up-converted OAM states after HD-FC. All of the units in beam profiles (c)–(l) are μm.

flat-top pump. We can find that SPCEs are flat for several low-OAM modes, i.e., $\ell = -2$ to 2, which are marked by the green box. However, in the situation of the Gaussian beam pump, there is a big gap in SPCEs among those OAM modes. Table I shows CEs of various frequency convertors for single-photon or entangled states. We see that the n-CEs converted by a flat-top beam near equally for different OAM states in five-dimensional space.

Figure 5(d) is the intensity of a flat-top beam profile in the center of crystal acquired by a CCD. Because of the imperfect alignment, the flat-top beam is not ideal. Nevertheless, the experimental results show unique advantages in OAM mode frequency conversion. Figures 5(e)–5(l) show the input (infrared) and output (visible) beam profiles of a single and superposed OAM states, respectively. We prepare the infrared OAM eigenstates of $|1\rangle$, $|2\rangle$, $|-1\rangle + |1\rangle$, and $|-2\rangle + |2\rangle$, respectively, which are shown in Figs. 5(e)–5(h). Figures 5(i)–5(l) show the corresponding visible beam profiles. The high similarity in the beam profile can directly illustrate the reliability of HF-FC.

APPENDIX B: QUANTUM STATE TOMOGRAPHY OF A QUDIT

For a qudit $|\psi\rangle_d = \frac{1}{\sqrt{d}} \sum_{\ell=-[d/2]}^{[d/2]} |\ell\rangle$, the density matrix can be written as

$$\rho = |\psi\rangle_d \otimes \langle\psi|_d, \tag{B1}$$

where each of the OAM eigenstates should be expressed as a vector in a d-dimensional space, i.e., $|-2\rangle = [1\ 0\ 0\ 0\ 0]^T$, $|-1\rangle = [0\ 1\ 0\ 0\ 0]^T$,..., $|2\rangle = [0\ 0\ 0\ 0\ 1]^T$ in a five-dimensional space. For a qudit state, using this definition, we can calculate the theoretical matrix of a qudit [43]. The density is a square matrix where each value is $1/d$. Experimentally, the density matrix of a qudit can be reconstructed by using high-dimensional quantum state tomography (QST) via mutually unbiased bases (MUBs),

$$\rho = \frac{1}{d} N \sum_{i,j=0}^{d^2-1} \left(A_i^j\right)^{-1} n_i \hat{\lambda}_j, \tag{B2}$$

where $\hat{\lambda}_j$ represents the elementary matrix associated with the SU(d) group, n_j is the coincidence count between the signal and heralding photon, and $A_i^j = \langle a_i|\hat{\lambda}_j|a_i\rangle$ is the measurement matrix associated with MUBs, $|a_i\rangle$.

The group of MUBs $\{|a_m^j\rangle\}$ can be generated using the Weyl group, Hadamard matrix, and Fourier Gauss transform methods. Here we used the discrete Fourier Gauss transform to product MUBs in prime-dimensional space [44],

$$\left\{\left|a_m^j\right\rangle\right\} = \left\{\frac{1}{\sqrt{d}} \sum_{n=0}^{d-1} \omega_d^{(jn^2+nm)} |n\rangle\right\}, \tag{B3}$$

where $j (j = 0 \ldots d-1)$ indexes the group of the MUBs, $m (m = 0 \ldots d-1)$ indexes the superposed OAM states for each set in MUBs, and $|\langle a_m^j | a_{m'}^{j'} \rangle|^2 = 1/d(1 - \delta_{jj'})$ for the

MUBs. In actuality, j runs from 0 to d, with the last set of MUBs being the OAM eigenstates:

$$\left\{\left|a_m^d\right\rangle\right\} \rightarrow \{|0\rangle, |1\rangle, \ \ldots \ |d-1\rangle\}. \tag{B4}$$

For a two-dimensional OAM space ($d = 2$), the eigenstates of three Pauli operators form a complete set of MUBs, which can be represented by the following Pauli matrices. The corresponding measured superposed OAM states are

$$\begin{aligned}
\{\mathrm{I}_1\} &= \{|0\rangle, |1\rangle\}, \\
\{\mathrm{I}_2\} &= \frac{1}{\sqrt{2}}\{|0\rangle + |1\rangle, |0\rangle - |1\rangle\}, \\
\{\mathrm{I}_3\} &= \frac{1}{\sqrt{2}}\{|0\rangle + i|1\rangle, |0\rangle - i|1\rangle\}.
\end{aligned} \tag{B5}$$

We can find that the number of MUBs is $d(d+1)$, while the elements of the density matrix are d^2. The reason is that these MUBs form an overcomplete tomography basis [55]. In principle, the density matrix can be reconstructed by Eq. (B2). However, the density matrix may not be a physical density matrix, i.e., it has the property of positive semidefiniteness. For overcoming this disadvantage, we employ the maximum-likelihood estimation method to estimate a physical density matrix [42,56],

$$L(t_1, t_2, \ldots, t_{d^2}) = \sum_{j=0}^{d^2-1} \frac{[N(\langle\Psi|_j \rho_{\exp} |\Psi\rangle_i) - n_j]^2}{2N(\langle\Psi|_j \rho_{\exp} |\Psi\rangle_i)}, \tag{B6}$$

where $|\Psi\rangle_j$ has the same meaning as the formula in Ref. [56].

[1] J. Huang and P. Kumar, Phys. Rev. Lett. **68**, 2153 (1992).
[2] Z.-Y. Zhou, S.-L. Liu, Y. Li, D.-S. Ding, W. Zhang, S. Shi, M.-X. Dong, B.-S. Shi, and G.-C. Guo, Phys. Rev. Lett. **117**, 103601 (2016).
[3] F. Steinlechner, N. Hermosa, V. Pruneri, and J. P. Torres, Sci. Rep. **6**, 21390 (2016).
[4] Z.-Y. Zhou, Y. Li, D.-S. Ding, W. Zhang, S. Shi, B.-S. Shi, and G.-C. Guo, Light: Sci. Appl. **5**, e16019 (2016).
[5] R. Ikuta, Y. Kusaka, T. Kitano, H. Kato, T. Yamamoto, M. Koashi, and N. Imoto, Nat. Commun. **2**, 537 (2011).
[6] M. T. Rakher, L. Ma, O. Slattery, X. Tang, and K. Srinivasan, Nat. Photonics **4**, 786 (2010).
[7] S. Tanzilli, W. Tittel, M. Halder, O. Alibart, P. Baldi, N. Gisin, and H. Zbinden, Nature (London) **437**, 116 (2005).
[8] R. Ikuta, T. Kobayashi, T. Kawakami, S. Miki, M. Yabuno, T. Yamashita, H. Terai, M. Koashi, T. Mukai, T. Yamamoto *et al.*, Nat. Commun. **9**, 1997 (2018).
[9] A. M. Yao and M. J. Padgett, Adv. Opt. Photonics **3**, 161 (2011).
[10] M. Erhard, R. Fickler, M. Krenn, and A. Zeilinger, Light: Sci. Appl. **7**, 17146 (2018).
[11] C. Godfrin, A. Ferhat, R. Ballou, S. Klyatskaya, M. Ruben, W. Wernsdorfer, and F. Balestro, Phys. Rev. Lett. **119**, 187702 (2017).
[12] A. Tavakoli, M. Pawlowski, and M. Bourennane, Ph.D. thesis, Master's thesis, Stockholm University, 2015.
[13] B. Perez-Garcia, R. I. Hernandez-Aranda, A. Forbes, and T. Konrad, J. Mod. Opt. **65**, 1942 (2018).
[14] L. Allen, M. W. Beijersbergen, R. J. C. Spreeuw, and J. P. Woerdman, Phys. Rev. A **45**, 8185 (1992).
[15] T. Giordani, E. Polino, S. Emiliani, A. Suprano, L. Innocenti, H. Majury, L. Marrucci, M. Paternostro, A. Ferraro, N. Spagnolo *et al.*, Phys. Rev. Lett. **122**, 020503 (2019).
[16] M. Mirhosseini, O. S. Magaña-Loaiza, M. N. O'Sullivan, B. Rodenburg, M. Malik, M. P. Lavery, M. J. Padgett, D. J. Gauthier, and R. W. Boyd, New J. Phys. **17**, 033033 (2015).
[17] N. J. Cerf, M. Bourennane, A. Karlsson, and N. Gisin, Phys. Rev. Lett. **88**, 127902 (2002).
[18] A. Sit, F. Bouchard, R. Fickler, J. Gagnon-Bischoff, H. Larocque, K. Heshami, D. Elser, C. Peuntinger, K. Günthner, B. Heim, C. Marquardt, G. Leuchs, R. W. Boyd, and E. Karimi, Optica **4**, 1006 (2017).
[19] D. Cozzolino, B. Da Lio, D. Bacco, and L. K. Oxenløwe, Adv. Quantum Technol. **2**, 1900038 (2019).
[20] G. B. Xavier and G. Lima, Commun. Phys. **3**, 9 (2020).
[21] D. Cozzolino, D. Bacco, B. Da Lio, K. Ingerslev, Y. Ding, K. Dalgaard, P. Kristensen, M. Galili, K. Rottwitt, S. Ramachandran *et al.*, Phys. Rev. Appl. **11**, 064058 (2019).
[22] H. Cao, S.-C. Gao, C. Zhang, J. Wang, D.-Y. He, B.-H. Liu, Z.-W. Zhou, G.-X. Zhu, Y.-J. Chen, Z.-H. Li *et al.*, arXiv:1811.12195.
[23] S.-L. Liu, S.-K. Liu, Y.-H. Li, S. Shi, Z.-Y. Zhou, and B.-S. Shi, Opt. Express **25**, 24290 (2017).
[24] B. Sephton, A. Vallés, F. Steinlechner, T. Konrad, J. P. Torres, F. S. Roux, and A. Forbes, Opt. Lett. **44**, 586 (2019).
[25] S. Kumar, H. Zhang, S. Maruca, and Y.-P. Huang, Opt. Lett. **44**, 98 (2019).
[26] L.-M. Duan, M. Lukin, J. I. Cirac, and P. Zoller, Nature (London) **414**, 413 (2001).
[27] D.-S. Ding, W. Zhang, Z.-Y. Zhou, S. Shi, G.-Y. Xiang, X.-S. Wang, Y.-K. Jiang, B.-S. Shi, and G.-C. Guo, Phys. Rev. Lett. **114**, 050502 (2015).
[28] D.-S. Ding, Z.-Y. Zhou, B.-S. Shi, and G.-C. Guo, Nat. Commun. **4**, 2527 (2013).
[29] N. Bozinovic, Y. Yue, Y. Ren, M. Tur, P. Kristensen, H. Huang, A. E. Willner, and S. Ramachandran, Science **340**, 1545 (2013).
[30] J. Wang, Photonics Res. **4**, B14 (2016).
[31] Y. Li, Z.-Y. Zhou, S.-L. Liu, S.-K. Liu, C. Yang, Z.-H. Xu, Y.-H. Li, and B.-S. Shi, OSA Continuum **2**, 470 (2019).
[32] N. Curtz, R. Thew, C. Simon, N. Gisin, and H. Zbinden, Opt. Express **18**, 22099 (2010).
[33] T. Kobayashi, R. Ikuta, S. Yasui, S. Miki, T. Yamashita, H. Terai, T. Yamamoto, M. Koashi, and N. Imoto, Nat. Photonics **10**, 441 (2016).
[34] M. Vasilyev and P. Kumar, Opt. Express **20**, 6644 (2012).
[35] R. W. Boyd, *Nonlinear Optics* (Elsevier, New York, 2003).
[36] K. Gillen-Christandl, G. D. Gillen, M. Piotrowicz, and M. Saffman, Appl. Phys. B **122**, 131 (2016).
[37] C. Brosseau, *Fundamentals of Polarized Light* (Wiley, New York, 1998).
[38] E. Bolduc, N. Bent, E. Santamato, E. Karimi, and R. W. Boyd, Opt. Lett. **38**, 3546 (2013).
[39] S.-L. Liu, Q. Zhou, S.-K. Liu, Y. Li, Y.-H. Li, Z.-Y. Zhou, G.-C. Guo, and B.-S. Shi, Commun. Phys. **2**, 75 (2019).

[40] A. Laskin, N. Šiaulys, G. Šlekys, and V. Laskin, *Laser Material Processing for Solar Energy Devices II*, Vol. 8826 (International Society for Optics and Photonics, Bellingham, WA, 2013), p. 88260F.
[41] H. Qassim, F. M. Miatto, J. P. Torres, M. J. Padgett, E. Karimi, and R. W. Boyd, JOSA B **31**, A20 (2014).
[42] S. Liu, Z. Zhou, S. Liu, Y. Li, Y. Li, C. Yang, Z. Xu, Z. Liu, G. Guo, and B. Shi, Phys. Rev. A **98**, 062316 (2018).
[43] R. T. Thew, K. Nemoto, A. G. White, and W. J. Munro, Phys. Rev. A **66**, 012303 (2002).
[44] M. Wieśniak, T. Paterek, and A. Zeilinger, New J. Phys. **13**, 053047 (2011).
[45] J. F. Poyatos, J. I. Cirac, and P. Zoller, Phys. Rev. Lett. **78**, 390 (1997).
[46] F. Bouchard, N. H. Valencia, F. Brandt, R. Fickler, M. Huber, and M. Malik, Opt. Express **26**, 31925 (2018).
[47] M. Krenn, J. Handsteiner, M. Fink, R. Fickler, and A. Zeilinger, Proc. Natl. Acad. Sci. USA **112**, 14197 (2015).
[48] C. Yang, S.-L. Liu, Z.-Y. Zhou, Y. Li, Y.-H. Li, S.-K. Liu, Z.-H. Xu, G.-C. Guo, and B.-S. Shi, Opt. Commun. **460**, 125143 (2020).
[49] L. Pattelli, R. Savo, M. Burresi, and D. S. Wiersma, Light: Sci. Appl. **5**, e16090 (2016).
[50] Z. Zhu, W. Gao, C. Mu, and H. Li, Optica **3**, 212 (2016).
[51] D. Naidoo, I. A. Litvin, and A. Forbes, Optica **5**, 836 (2018).
[52] J. Bovatsek and R. S. Patel, *International Congress on Applications of Lasers & Electro-Optics* (Laser Institute of America, Orlando, FL, 2007), Vol. 2007, p. M806.
[53] A. Laskin, V. Laskin, and A. Ostrun, *Laser Beam Shaping XVII*, Vol. 9950 (International Society for Optics and Photonics, Bellingham, WA, 2016), p. 995002.
[54] S. A. Collins, JOSA **60**, 1168 (1970).
[55] D. Giovannini, J. Romero, J. Leach, A. Dudley, A. Forbes, and M. J. Padgett, Phys. Rev. Lett. **110**, 143601 (2013).
[56] D. F. V. James, P. G. Kwiat, W. J. Munro, and A. G. White, Phys. Rev. A **64**, 052312 (2001).